Applied Catalysis B: Environmental 342 (2024) 123426

Contents lists available at ScienceDirect

Applied Catalysis B: Environmental

journal homepage: www.elsevier.com/locate/apcatb

Sustainable ammonia production via nanosecond-pulsed plasma oxidation and electrocatalytic reduction

Jing Sun [a,b], Renwu Zhou [a,*], Jungmi Hong [c], Yuting Gao [a], Zhongping Qu [a], Zhijie Liu [a], Dingxin Liu [a], Tianqi Zhang [c], Rusen Zhou [c], Kostya (Ken) Ostrikov [d], Patrick Cullen [c], Emma C. Lovell [b], Rose Amal [b], Ali Rouhollah Jalili [b,*]

[a] State Key Laboratory of Electrical Insulation and Power Equipment, Centre for Plasma Biomedicine, School of Electrical Engineering, Xi'an Jiaotong University, Xi'an, Shaanxi 710049, People's Republic of China
[b] School of Chemical Engineering, University of New South Wales (UNSW), Sydney, NSW 2052, Australia
[c] School of Chemical and Biomolecular Engineering, University of Sydney, Sydney, NSW 2006, Australia
[d] School of Chemistry and Physics and QUT Centre for Materials Science, Queensland University of Technology (QUT), Brisbane, QLD 4000, Australia

ARTICLE INFO

Keywords:
Ammonia
Plasma bubbles
Electrocatalysis
Reaction mechanisms

ABSTRACT

The production of ammonia, powered by renewable energy, in a decentralized manner is of key importance in the transition to a more sustainable future. Recent research has explored the integration of non-thermal plasma and electrochemical processes to achieve this goal. However, the success of this hybrid process is contingent on the energy efficiency of the plasma-generated species. Herein, we developed a plasma bubble reactor, driven by nanosecond pulses interfacing plasma directly with water. This reactor can comprehensively probe gas ionization processes, different energy channels, corresponding plasma catalytic reaction mechanisms, and reactive species in gas and liquid phases. By using on-and-off plasma ignition with rapid pulses, we could regulate energy consumption in cycles and achieved the lowest reported energy consumption of 2.7 ± 0.1 kWh mol^{-1} NO_3^- and 3.2 ± 0.1 kWh mol^{-1} NH_4^+ after electrocatalytic nitrate reduction. This provides a promising pathway to producing green, renewable ammonia from air and water.

1. Introduction

Ammonia is the second most produced chemical worldwide and is essential in providing food for over half of the global population [1]. Its potential as a hydrogen carrier is significant for the emerging global hydrogen transport economy [2]. Nonetheless, the existing ammonia synthesis technology, the Haber-Bosch (H-B) process, accounts for over 2% of worldwide CO_2 emissions and approximately 5% of annual natural gas consumption [3]. Furthermore, due to its high temperature and pressure requirements, the H-B process can only be utilized in large-scale, centralized production approaches that demand significant infrastructure [4]. With increasing awareness of climate change, there is a growing demand for low-carbon-emitting alternatives that do not heavily rely on fossil fuels [5]. As a result, there has been a considerable increase in intensive research efforts aimed at improving and decentralizing ammonia production via renewable electricity-powered technologies, such as plasma and electrochemical methods [6,7]. However, converting atmospheric nitrogen to ammonia remains a significant challenge when independently utilizing electrochemical, thermal, or non-thermal plasma processes. For direct electrochemical nitrogen reduction reactions, the low reactivity of atmospheric nitrogen and its insolubility in conventional reaction media has resulted in negligible ammonia production rates and selectivity [8]. Direct conversion of atmospheric nitrogen and hydrogen to ammonia with plasma requires a significant amount of energy and has a low product selectivity [9,10]. This is because dissociating N_2 molecules through plasma whilst preventing the decomposition of produced ammonia is difficult to achieve [11].

Our recent finding highlighted the importance of integrating non-thermal plasma (NTP) with electrocatalysis to tackle the above challenges [12]. NTP generates highly energetic electrons to produce reactive and soluble nitrogen intermediates in water [13]. The subsequent electrocatalytic conversion of plasma-generated species (NO_3^- and NO_2^-) drives the selective production of ammonia under mild conditions.

* Corresponding authors.
E-mail addresses: renwu.zhou@xjtu.edu.cn (R. Zhou), ali.jalili@unsw.edu.au (A.R. Jalili).

https://doi.org/10.1016/j.apcatb.2023.123426
Received 12 July 2023; Received in revised form 6 October 2023; Accepted 21 October 2023
Available online 25 October 2023
0926-3373/© 2023 The Author(s). Published by Elsevier B.V. This is an open access article under the CC BY license (http://creativecommons.org/licenses/by/4.0/).

Unlike the strong N≡N bond (941 kJ mol^{-1}) in atmospheric N_2, the N = O bond in NTP generated NO_x^- has a lower dissociation energy (204 kJ mol^{-1}), making electrocatalytic ammonia production practical [14]. Although it may not yet match the productivity of the established H-B process, it has already shown great potential for transforming ammonia production in a more sustainable and environmentally friendly manner [15–17]. In addition, the underlying mechanism of plasma activation remains largely unknown, which presents a unique opportunity for significant advancements in green ammonia synthesis.

Recent research has shown that the use of NTP in a bubble reactor, which delivers plasma-activated air directly into the water, can significantly enhance the effectiveness of the air activation process [12]. This is because the activated nitrogen molecules can directly interface with water, resulting in a direct reaction between ionized nitrogen and nitrogen oxides with water. This enhanced reaction led to a five-fold increase in the production rate of NO_x^- in water [12]. Furthermore, recent advancements in incorporating catalysis into NTP-bubble reactors have further demonstrated the viability of utilizing multiple discharges for nitrogen fixation at ambient pressure and temperature [9]. Notably, producing reactive species resulting from plasma-water interactions can depend strongly on the excitation techniques. The use of pulsed plasma activation of air, primarily through nanosecond pulses, has become increasingly popular due to its high energy efficiency compared to other methods, such as AC or DC high voltage [18,19]. This approach offers benefits such as enhanced discharge stability and controllability and minimizing energy losses typically resulting from heating gas molecules [18]. The nanosecond pulsed power effectively drives plasma chemistries by promoting ionization during discharge initiation and facilitating a highly non-equilibrium electron energy distribution [20–22].

Achieving energy optimization when using nanosecond pulsed plasma for N_2 fixation in liquids is a complex and critical task, especially when pairing the plasma with an electrolyzer for scalable ammonia synthesis. Numerous studies have delved into the potential of nanosecond pulsed plasma for a wide range of applications, from environmental and biomedical uses [23,24], to materials modification [25,26], and gas conversions [27–29]. These studies have shown promising results in terms of energy efficiency, as they prevent gas overheating and coking processes. Dry reforming of natural gas and CO_2 has also been successfully investigated [28]. Despite this progress, while most studies have focused on gas phase analysis via nanosecond pulses, only a few reports have examined the use of gas-to-liquid discharge preferred for transferring activated nitrogen into the liquid phase [30]. Moreover, the plasma needed for nitrogen fixation differs significantly from the plasma used predominantly in most studies that activate oxygen to produce ozone in a dielectric barrier discharge (DBD) plasma [31]. The challenge lies in the energy of the N triple bond, the overall production rate, and the energy consumption required to sustain the plasma. Compared to ozone production, the input energy via pulse must be tuned more critically as many more potential energy channels are possible. Therefore, apart from the direct breaking of triple N bonds, energy can be wasted through various excitation, dissociation, and solvation processes. Systematic experimental analysis and modelling across multiple plasma modes are required to fully comprehend how nanosecond pulses can drive N_2 fixation in liquids for high productivity and energy efficiency. The ultimate goal is to identify the most effective plasma process for industrial-scale adoption of the hybrid-plasma electrocatalysis for green ammonia synthesis, which will cut costs and maximize productivity.

This study aims to enhance the energy efficiency of the plasma-electrocatalysis system for sustainably producing NH_3 directly from air and water using the N_2-NO_x-NH_3 pathway, by regulating both the chemistry and energy input through nanosecond pulsed plasma. It also discusses how to match the productivity of plasma reactors with the required physicochemical characteristics of the electrocatalyst and ammonia electrolyzer. The development also aligns the synthesis of efficient copper catalysts for ammonia production with the simultaneous production of plasma-generated NO_x. To achieve this, we developed a nanosecond pulse-driven plasma bubble reactor with multiple discharge schemes that enable independent ignition and comparison of multiple discharges. Our investigation focuses on two primary modes observed in plasma-bubble discharges, DBD and SD (spark discharge), to increase the production rate of reactive nitrogen species for subsequent electrocatalytic reactions. We use an intensified charge-coupled device (ICCD) and a digital oscilloscope to study the evolutionary processes of these discharge modes and better regulate the energy input for maximum efficiency. In-situ optical emission spectra (OES) and Fourier Transform infrared spectroscopy (FTIR) are used to determine the composition of the gaseous plasma. We analyze the impact of discharge modes on plasma-liquid interactions concerning the physio-chemical properties and concentration of NO_3^-. We also model the electron energy and chemistry of plasma bubbles to enable effective system matching for the subsequent electrochemical ammonia production. In addition to exploring the effectiveness of the different discharge schemes, we provide insights into the reaction mechanisms involved in the plasma-driven nitrate and ammonia production process. By Zero-D plasma chemistry modelling and comparing the energy costs of different NTP discharges, we identify the most energy-efficient approach to NO_3^- production, which leads to developing more sustainable and environmentally friendly methods for ammonia synthesis.

2. Experimental section

2.1. Plasma system setup and diagnostics

2.1.1. Plasma experimental setup

The experimental setup with diagnosis systems is shown in Fig. 1, consisting of a nanosecond pulse power supply (Smart Maple HV-2015, China), a plasma bubble reactor (Plasmaleap Technologies, Sydney) and electrical and optical diagnostic systems. The power source can provide an adjustable pulse repetition frequency with a range between 0 and 10 kHz and a voltage of up to 20 kV with a rising time of 11 μs and a pulse width of 15 μs. In this study, the reference discharge parameters were set at 6 kHz, 40 ns for pulse rise and fall time, and the pulse duration was set at 1μs. The applied voltage was set at the point where the discharge was initiated and stable, and the details were analyzed in Fig. S1. The bubble reactor consists of a cylindrical quartz tube (height: 200 mm) with 8 micro holes (diameter: 500 μm) evenly distributed around the outer quartz tube bottom to allow the gas to flow through the tube and diffuse into the water. A stainless-steel electrode (diameter: 1.8 mm) was placed in the water reservoir as the ground electrode. During the experiment, the reactor was submerged in a double-layered beaker containing 200 mL deionized water (DI water) with a depth of 15 cm (Fig. 2(b-d)). Water is also used as the absorber for DBD discharge and provides the liquid interface for interaction with spark discharge. The air gas is introduced into the reactor from the top, and its flow rate is controlled by a mass flow controller (Sevenstar D07–26) at 1 L/min in this experiment. The reactor temperature was controlled at 20 °C by a cooling water system.

2.1.2. Plasma electrical and optical measurements

Schematics of the two discharge mode configurations are shown in Fig. 2(c-d). The discharge modes were controlled by adjusting the distance between the high-voltage electrode tip and the level of the micro holes. In the DBD mode, the distance was set at 1 cm. The SD occurred at the same level as the micro holes with a quartz dielectric covering the stainless-steel rod to prevent DBD from occurring. To investigate the electrical characteristics of both designs, the electric parameters were recorded simultaneously by a digital oscilloscope (Tektronix, DPO3052). The pulse voltage was detected by a high-voltage probe (Tektronix P6015A), and the current was measured by a current probe (Tektronix, P6139A). The time-averaged discharge power (P) was calculated from the measured discharge voltage and current with Equation S1.

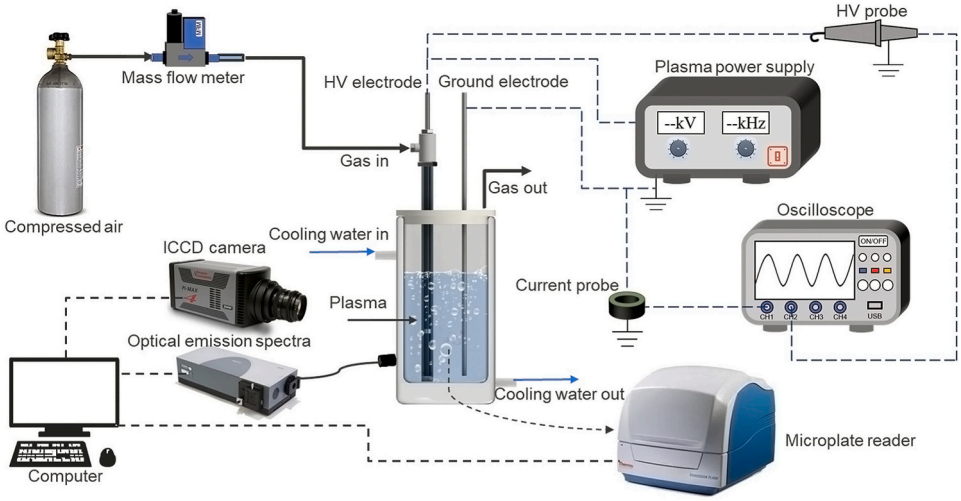

Fig. 1. Schematic diagram of the experimental devices and analysis systems.

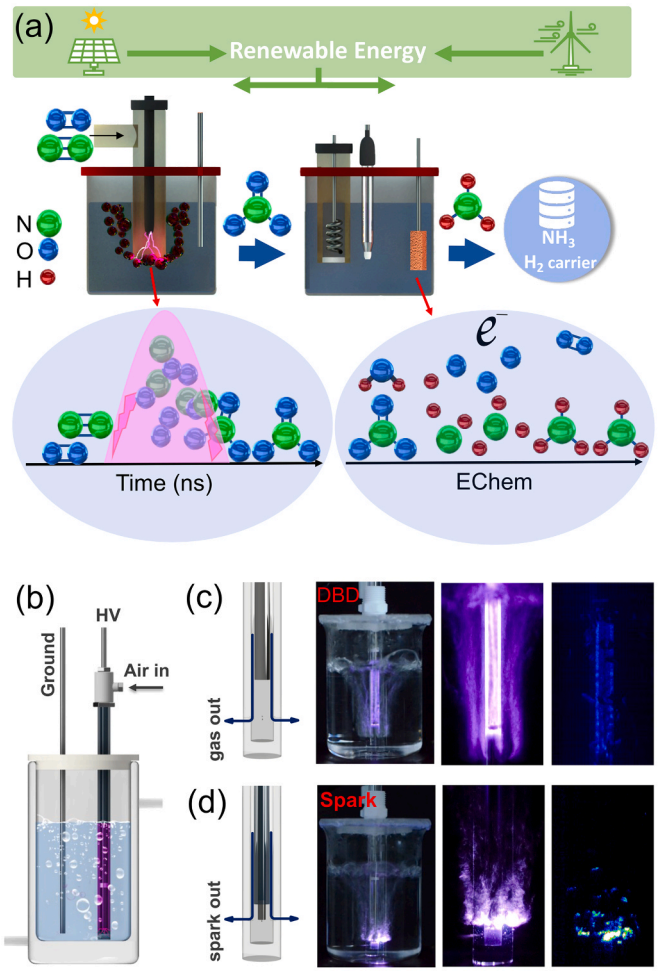

Fig. 2. (a) Schematic illustration of the hybrid plasma-electrocatalysis process and the system overview of the setup used to produce green ammonia. The electrochemical process is driven by renewable energy (electricity), while the nanosecond pulse power supply is used for plasma generation. (b) Schematic illustration of the bubble reactor configuration used in this study, as well as digital discharge images of various reactor configurations. (c) Time-integrated ICCD image with a 1 ms gate width of the dielectric barrier discharge (DBD) in the bubble reactor. (d) Time-integrated ICCD image with a 1 ms gate width of the spark discharge (SD) in the bubble reactor.

$$P = f\int_{t_0}^{t_0+T} u(t)i(t)dt \quad (1)$$

The discharge images were captured by a digital camera (Nikon D7000) with an exposure time of 1 s. An intensified charge-coupled device (ICCD) camera (PI-MAX3; Princeton Instruments) was placed facing the discharge area and 40 cm away from the experimental setup from the side to monitor the spatial-temporal evolution of the discharge region. Optical emission spectra (OES) were collected with an Andor SR-750i monochromator (grating grooving 1200 lines mm^{-1}). With the detected spectral range between 300 and 800 nm.

2.2. Electrochemical system

2.2.1. Copper nanoparticles fabrication

The commercial Cu mesh was cut into desired sizes and ultrasonically cleaned with acetone, ethanol, and Milli-Q water for 15 min intervals, and then washed with dilute H_2SO_4 solution to remove any surface impurities and oxide layers. A facile electrodeposition synthesis approach was adopted to prepare our catalyst. We electrodeposited Cu from a 50 mM $CuSO_4$ electro bath onto a cleaned Cu mesh substrate at − 1 V vs. Ag/AgCl for 300 s

The morphology and structure of Cu nanoparticles were imaged by scanning electron microscopy (SEM) using a JEOL JSM-IT-500 HR.

2.2.2. Electrochemical evaluation

All electrochemical assessments were conducted using CHI Potentiostat (CHI 760E) in a custom-designed H-type electrochemical cell. The cathodic chamber was separated from the anodic chamber by Nafion@ 117. A three-electrode setup with the Cu-based catalyst (as the working electrode (WE), platinum plate as the counter electrode (CE) and Ag/AgCl (*sat.* KCl) as the reference electrode (RE) was used. This study used Plasma-activated water as the nitrate-containing electrolyte (pH = 2). In a typical test, 50 mL of electrolyte was used in the cathodic chamber of the H-type cell to allow for electrolyte sampling. The electrode size for the H-cell was 1 $cm^{2,}$ and Cu catalyst was used for ammonia synthesis at − 0.5 V vs. RHE. The reaction was facilitated with a magnetic stirrer at 650 rpm.

2.3. Product detection and analysis

The main long-lived aqueous RONS (NO_3^-, NO_2^-, H_2O_2 and NH_4^+) are quantified by using spin trapping agents, which are Nitrate/Nitrite Colorimetric Assay Kit (Cayman, 780001, USA), Griess reagent Kit (Beyotime, S0021, China) and Peroxide Assay Kit (Beyotime, S0038,

China), indophenol blue detection method [12], respectively and a microplate reader (Thermo Scientific Varioskan Flash, USA). The indigo colorimetric method (Ozone AccuVac R Ampules, Hach 2516025, SA) is employed to detect the concentration of O_3 in the liquid phase with a visible spectrophotometer (Hach DR3900, USA). Milli-Q water with a resistivity of 18.2 MΩ.cm was obtained from an inline Millipore RiOs/Origin H_2O purification system, which was used throughout the experiments for sample preparation and reaction. The compositions of the effluent gases after passing through the water are analyzed by a Fourier-transform infrared (FTIR) spectrometer (Bruker, Tensor II).

2.3.1. Total nitrate + nitrite (NO_3^- + NO_2^-) detection by Nitrate Reductase and Griess Reagent

80 μL of the sample or sample dilutions was transferred into the wells on the sample plate, 10 μL of the Enzyme Cofactor Mixture and 10 μL of the Nitrate Reductase Mixture, respectively. Cover the plate, and the mixture was incubated at room temperature in the dark for one h to ensure all the nitrate was reduced to nitrite. After the required incubation time, add 50 μL of Griess Reagent R1 to each sample and immediately add 50 μL of Griess Reagent R2. Allow the colour to develop for 10 min at room temperature. Read the absorbance at 540 nm using the microplate reader. Solutions of HNO_3 with known concentrations were used as calibration standards, with the absorbance at 540 nm used to plot the calibration curves. The upper LOD of UV-Vis used in this study refers to the absorbance at 540 nm obtained from 100 μM HNO_3. A dilution factor was applied to measure nitrite concentration in plasma-activated water (PAW).

2.3.2. Nitrite (NO_2^-) detection by Griess Reagent

50 μL of the sample or sample dilutions was taken and transferred into the wells on the sample p, late, and 50 μL of Griess Reagent R1 was to each of the samples, then immediately add 50 μL of Griess Reagent R2. Allow the color to develop for 10 min at room temperature. Read the absorbance at 540 nm using the microplate reader. Solutions of HNO_2 with known concentrations were used as calibration standards, with the absorbance at 540 nm used to plot the calibration curves. The upper LOD of UV-Vis used in this study refers to the absorbance at 540 nm obtained from 100 μM HNO_2. A dilution factor was applied to measure nitrite concentration in plasma-activated water (PAW).

2.3.3. Ammonia (as ammonium NH_4^+) detection by the indophenol blue method

From the cathodic chamber electrolyte solution, 0.5 mL of electrolyte was taken and transferred into a 2 mL sample tube. Into the tube, 0.4 mL of 1 M NaOH solution (with 5 wt% salicylic acid and 5 wt% sodium citrate), 0.1 mL of 0.05 M NaClO and 30 μL of 1 wt% $C_5FeN_6Na_2O$ (sodium nitroferricyanide) in water was added. The mixture was then incubated in the dark at room temperature for one h before reading its absorbance. The concentration of ammonia was determined via a calibration curve. The calibration curve was prepared using a set of standard solutions with a known amount of $(NH_4)_2SO_4$ (concentrations were based on NH_4^+) in Milli-Q water. Into these solutions, the indophenol as mentioned above blue reagents were added, and the indophenol blue absorbance at 655 nm was determined after 1 h. The limit of detection (LOD) of UV-Vis used in this study refers to the absorbance at 655 nm obtained from blank Milli-Q water for the lower limit and 200 μM NH_4^+ for the upper limit.

2.3.4. Physiochemical properties measurements

The pH value, the oxidation-reduction potential (ORP) value and the conductivity of the plasma-treated solution are measured by a laboratory pH tester (METTLER-TOLEDO, FE20), a benchtop ORP meter (METTLER-TOLEDO, S210-K) and a conductivity tester (REX, DDS-307A), respectively.

2.4. Zero-D plasma chemistry modelling

A computational study utilizing a global plasma model and a water chemistry model was conducted to comprehend the diverse features of Spark and DBD discharges, as well as their distinct effects on NO_x^- synthesis. A zero-D plasma kinetic model for catalytic NO_x synthesis developed using open-source ZDPlaskin [32], was adapted for this comparative study between Spark and DBD conditions. A set of reaction equations related to $N_2/O_2/H_2O$ interactions are modified from the previous N_2/O_2 and N_2/H_2O models [33]. This was done due to the high possibility of sputtered and evaporated H_2O molecules in the Spark discharge, as observed in other studies on plasma-water interaction within the bubble [34]. However, for the simulation of the DBD condition, only an N_2/O_2 mixture was used in the gas discharge kinetics, with no assumptions made about added water molecules due to their indirect interaction with the water interface through the recombination zone.

The input reaction data was processed by the built-in preprocessor of the ZDPlasKin module, which converted it into coupled differential equations sorted into source and loss terms for individual species. These equations were then solved using the combined Boltzmann equation solver, BOLSIG+ [35], which provided reaction coefficients for various electron interactions and electron energy distribution, as described elsewhere [33]. The water chemistry model was used to simulate chemical reactions in liquid water volume, following the methodology and suggested reactions from Leitz and Kushner [36], where different solvation properties of different gas species were considered at the plasma-water interface.

Considering the direct interaction of active Spark discharge through the bubble interface, efficient electron and ionic species supply transport is expected by allowing entire transport without reflection loss [36]. Fast charge transfer into other neutrals in the aqueous phase may follow, mostly the majority of H_2O molecules at first and redistribute to other aqueous species such as $O^-_{2(aq)}$ or $OH^-_{(aq)}$. In general, for the neutral species, the number density of the corresponding aqueous phase species was to be limited by the finite solubility with certain reflection loss. Unlike Spark discharge, in DBD discharge configuration, plasma species pass a certain recombination zone, which may lose reactive species such as atoms and radicals as well as ionic species [36].

2.4.1. Estimation of input parameters of reduced electric field E/N and electron density n_e

The highly transient characteristics of spark discharge result in difficulties in estimating important input parameters such as reduced electric field E/N and electron density n_e, as well as discharge volume, hence the residence time of molecules within the discharge. The cross-sectional discharge area and the discharge volume for the Spark discharge were estimated as 6.25×10^{-2} cm^2 and 6.25×10^{-2} cm^3, respectively, based on the assumption of 8 ea of 1 mm diameter of the Spark discharge column considering the eight-gas channel through the quartz tube wall. Although the diameter of the through hole on the quartz tube reactor wall is 200 μm, considering the expanded spark area inside the reactor tube and at the bubble, this estimation is more acceptable. However, it needs special attention because it may contain significant errors and influence the estimation of all related parameters, such as current density and power density. Therefore, the modelling result, especially on Spark discharge condition, must be treated as a more qualitative evaluation to understand overall different characteristics and pathways to produce NO_x^- compared to DBD.

Conventional methodology to extract E/N using a QV(Charge-Voltage) Lissajous plot [37] was unavailable with this fast-rising square pulse power condition. Alternatively, integrated net charge density from the measured current profile was used to estimate the approximate electron density level [38]. The initial guess of electron density was estimated using Eqs. (2) and (3). The conduction current J_c, is obtained from integrated net charge value Q from the measured current result and the estimated discharge and period cross-sectional area.

The initial reduced electric field value was assumed as 210 Td and 360 Td at gas temperature 300 K conditions for Spark and DBD discharge, respectively, from which its rms voltage was taken as the initial guess of electric potential. However, it is known that as breakdown occurs, free electrons and ions form the opposing field against the externally applied electric field, which results in a significantly reduced electric field during the discharge pulse [39]. Especially for Spark discharge with high-density electrons, the actual discharge voltage can be lowered considerably; hence the reduced electric field E/N can be considerably low in comparison to DBD with a similar applied power condition [40].

$$J_c^e = -n_e e \mu_e E \tag{2}$$

$$J_c^e = -\Delta Q / (A \Delta T) \tag{3}$$

where e, μ_e, E, A and ΔT indicate unit electron charge, electron mobility, electric field strength, cross-sectional discharge area and time.

Through preliminary modelling over the ranges of electron density and reduced electric field, the required reduced electric field E/N was chosen best to match the peak power and current density level, as summarized in Table S1.

3. Results and discussion

3.1. Productivity

The production of NO_x^- through pulsed plasma from air heavily relies on the excitation of nitrogen molecules and energy distribution across various plasma regimes. A deeper understanding of these processes requires a detailed investigation of DBD and SD separately. By analyzing these discharges individually, we can identify the activation mechanisms of nitrogen molecules and the energy contribution of each plasma regime. To enhance the effectiveness of this controlled excitation mechanism, we can establish correlations between plasma regimes and subsequent electrochemical processes while considering energy barriers.

Fig. 2a and b illustrate our process and reactor in schematic diagrams. We could switch between different discharge modes by modifying the electrode configuration in our plasma bubble reactor. Fig. 2(c-d) depicts that the electrode configurations and the corresponding digital discharge images differed for DBD and SD. In a DBD, a uniform discharge plasma consisting of intense filamentary discharges between the two dielectric tubes was typically observed under a large gas gap. In contrast, under a small gas gap, plasma discharges generated within the continuously forming underwater bubbles are enabled using relatively high-energy plasma modes associated with SD. At the plasma-liquid interface (PLI), this SD generated in the forming gas bubbles offered a large specific surface area. This increases the probability of forming reactive species in the liquid phase, which will be discussed in greater detail later. On the other hand, the DBD generated in the quartz tube could activate the feed gas and transfer the gaseous species into the solution. Moreover, the high-quality spectra images of 1 ms gate width acquired by ICCD demonstrated that the spark discharges persisted inside the bubbles after being released from the micro holes and away from the electrode (Fig. 2d).

In order to better understand the production of reactive gaseous species in the discharge zones and to obtain information on the energy distribution within the plasma, we conducted in situ optical emission spectroscopy (OES), as shown in Fig. 4(a-b). By understanding the energy distribution, we may adjust the plasma conditions to enhance the production of NO_x^- and minimize the formation of undesired species. High-intensity optical emission of N_2 SPS (Second Positive System N_2(C3->B3)) and N_2 + FNS (First Negative System, N_2 +(B->X) indicates the high concentration of electronically excited nitrogen molecules and ions in DBD, which results from energetic electron collisions with O_2 and N_2 molecules. The N_2 ($B^3\Pi$ and $C^3\Pi$) and N_2^+ ($X^2\sum_g^+$) states are mainly produced from the electron-impact excitation of the molecular ground state N_2 ($X^1\sum_g^+$). The energetic collisions of electrons with O_2 molecules ($O_2 + e^- \rightarrow 2\bullet O + e^-$) account for the formation of •O radicals with the optical emission at 777.2 nm. In contrast, the optical spectra measured from the pulsed SD within the bubbles include additional •OH emission lines. •OH radicals with optical emission at 309 nm are generated primarily by the electron impact dissociation of water molecules at the SD interface ($H_2O + e^- \rightarrow \bullet H + \bullet OH + e^-$).

Gas temperature is a crucial parameter to govern chemical reactions in the gas phase as it significantly impacts plasma chemistry, which drives most plasma-enabled applications [41]. The vibrational temperature (T_{vib}) serves as an indicator of energy distribution between different vibrational states, which is related to the electron temperature in the discharge region. It is also important to note that different gas compositions and temperatures can influence T_{vib} through vibrational-translational and vibrational-vibrational interactions. In contrast, the rotational temperature (T_{rot}) of excited states is commonly assumed to be a reasonable indicating value of gas temperature at atmospheric pressure [42]. Electron collisions mainly govern vibrational transitions, while collisions with heavier particles control rotational transitions because electrons cannot provide enough rotational energy to molecules due to their small masses. As a result, electron energy can be transformed into vibrational energy, while collision relaxation between vibration-excited molecules can generate rotational energy [42]. The population distribution in rotational levels of excited states of diatomic molecules is typically used in emission spectroscopy to obtain gas temperature measurements in non-equilibrium plasmas. These measurements are taken from excited states of diatomic molecules.

To determine T_{vib} and T_{rot} values of both DBD and SD, the OES of the N_2 second positive system is used by comparing the calculated spectra of the $C^3\Pi_u - B^3\Pi_g$ ($\Delta v = -2$) band transition of excited nitrogen with the experimental data, which was achieved by using the software Specair. The simulation result in Fig. 3(c-d) shows the best-fitting simulation spectra to the observed spectra of N_2(C–B) emitted from both discharges. It shows that the simulated spectra at $T_{vib} = 2900$ K and $T_{rot} = 400$ K fit the experimental DBD spectra well, while $T_{vib} = 3100$ K and $T_{rot} = 950$ K are achieved in the SD. DBD and SD exhibit a non-thermal equilibrium state, as evidenced by their higher vibrational temperatures than their rotational temperatures [43]. Notably, the SD exhibits a higher T_{vib} than DBD, which suggests higher relative concentration of high-lying vibrationally excited states. It can be beneficial to enhance certain chemical reactions requiring high activation energy [44]. Consequently, when subjected to identical pulse conditions, the SD is anticipated to generate considerably higher levels of NO_x^-, as elaborated upon below. In addition, the much higher T_{rot} of SD suggests high gas temperature, which improves the overall chemical reaction rate because it affects the alignment and collision patterns of gas molecules in the spark and at the interface with water, influencing the likelihood of successful reactions.

As well as high gas temperature, a significantly higher relative ratio of N_2^+(B->X) emission intensity against N_2 SPS and estimated high T_{vib} suggests the presence of high-density high energy electrons in SD. When discharge energies increase, the number, density and energy of electrons may also increase, leading to a rise in vibrational energies and, consequently, higher rotational energies. Therefore, in generating nitrogen oxides using plasma air activation, the temperature of molecular vibration (T_{vib}) plays the primary role. The creation of NO_x^- requires breaking the bonds between nitrogen and oxygen atoms and forming new bonds between N and O atoms. Based on the active O- and N-species described earlier and the possible reaction pathways reported in the literature, the chemical reactions and mechanisms for DBD and SD are described below. In the gas phase, energetic electrons generated by plasma collide with O_2 and N_2, dissociating the gas molecules to form N and O atoms:

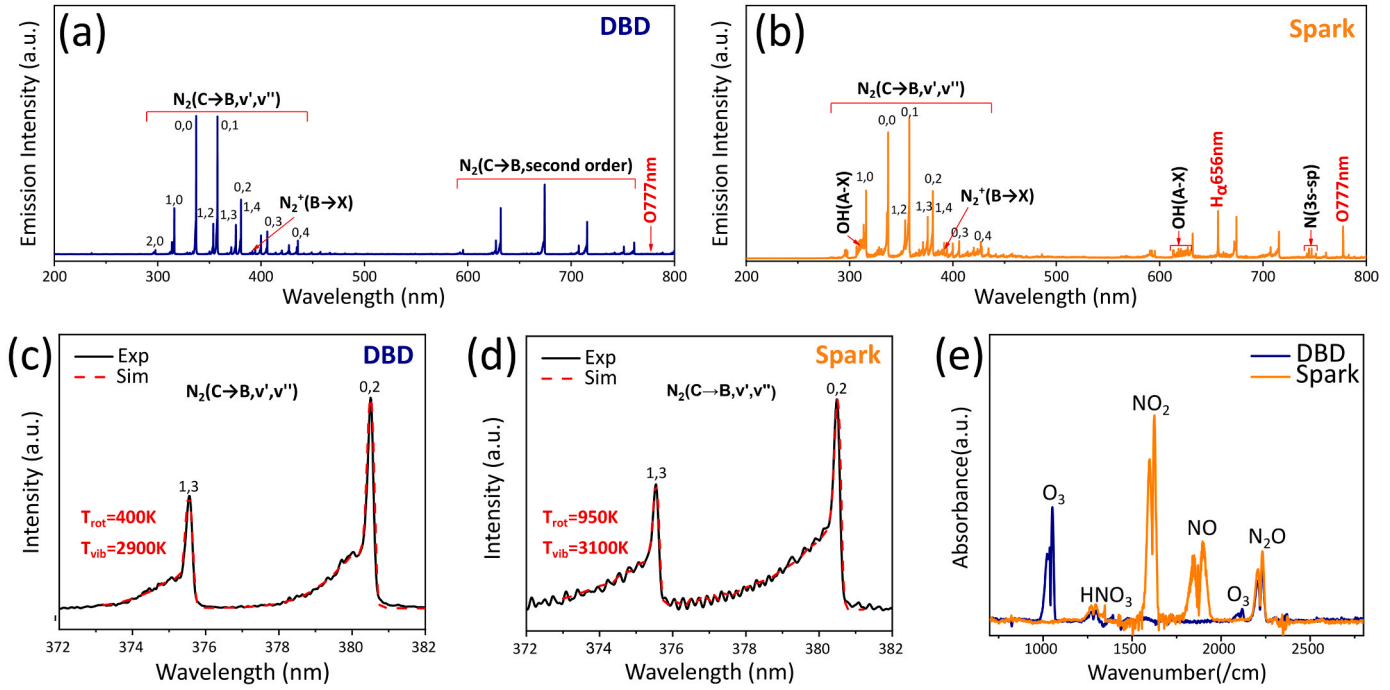

Fig. 3. The optical emission spectra of (a) DBD mode and (b) SD mode from 200 nm to 800 nm; the determination of T_{rot} and T_{vib} by curving fitting of the nitrogen second positive system for (c) DBD mode and (d) SD mode; (e) FTIR spectra of the outlet gaseous products.

$$e^- + N_2 \leftrightarrow N + N + e^- \quad \text{(R1)}$$

$$e^- + O_2 \leftrightarrow O + O + e^- \quad \text{(R2)}$$

New bond-forming reactions depend on the molecules' vibrational energy in the next step. The dominant chemistry for NO_x production in the atmospheric pressure air plasma proceeds via a vibrationally enhanced Zeldovich mechanism consisting of the following reactions:

$$N + O_2 \quad /O_2 \quad (v) \leftrightarrow O + NO \quad \text{(R3)}$$

$$O + N_2 \quad /N_2(v) \leftrightarrow N + NO \quad \text{(R4)}$$

In the vibrationally enhanced Zeldovich mechanism, the N_2 molecules become vibrationally excited through collisions with energetic electrons produced by the plasma. This increased vibrational energy lowers the energy threshold required to break the strong N_2 triple bond (9.8 eV). The vibrationally excited N_2 molecules can then collide with O atoms and dissociate, forming reactive N and O atoms. The N atoms formed in R1 can further react with ground-state and vibrationally excited O_2 molecules (R3 and R4) to produce another NO. Reaction 2 also creates an additional O atom, which can again react with ground-state and vibrationally excited N_2 molecules, providing a tightly coupled reaction loop.

However, at this point, preventing the excessive accumulation of NO becomes essential because it could stimulate reverse reactions of R3 and R4. It is interesting to note that the forward reaction of R3 is temperature-independent while the backward reaction is not. Utilization of pulsed plasma that generates plasma on/off results in a successively hot and cold environment, which can serve as the foundation for the high productivity of the pulsed plasma developed here due to this difference in the kinetics of forwards and backward reactions in the R3. N, $N_{2\ (g,v)}$, $O_{2\ (g,v)}$, and O are produced when air enters the plasma region. Since the forward reaction of R3 has significantly faster kinetics than R4, it becomes the dominant reaction, resulting in significant NO and O production. Notably, the reverse reaction of R4 is independent of temperature, but it is unlikely to occur initially due to the consumption of N by R3 and the low NO concentration. As R3 advances, the population of O (from plasma and R3's byproduct of the forward reaction) increases, which can destroy NO as R3's reverse reaction becomes dominant. Due to its dependence on high temperature, the backward reaction of R3 cannot destroy the produced NO when the plasma is turned off (in between the pulses). Despite the high concentrations of O and NO, the reverse reaction of R3 does not occur in this instance. Instead, the excess O drives the forward reaction of R4, which increases NO and N production. Utilizing the produced $N_{2(v)}$ and O, pulse plasma promotes forward reactions while inhibiting R3's reverse reactions. Subsequently, the NO made in both pathways has sufficient time to undergo further oxidation via interaction with O and $O_{2(g,v)}$ atoms (R5 and R6) to produce NO_2.

$$NO + O \leftrightarrow NO_2 \quad \text{(R5)}$$

$$2NO + O_2 \leftrightarrow 2NO_2 \quad \text{(R6)}$$

However, if the gas temperature is not high enough, oxygen molecules (O_2) dissociation to form reactive oxygen atoms (O) may also not occur optimally. In this scenario, instead of NO_2, ozone (O_3), as an unwanted product, may be formed in high number density by reacting O atoms with O_2 molecules (R6).

$$O + O_2 \quad /O_2 \quad (v) \leftrightarrow O_3 \quad \text{(R7)}$$

Fig. 3(e) shows FTIR spectra of the outlet gaseous products, confirming ozone formation as the primary product in the DBD discharge. The formation of ozone instead of NO/NO_2 can be attributed to insufficient gas temperature, highlighting the importance of selecting an appropriate discharge scheme for plasma air activation to achieve the desired chemistry. While pulsed plasma DBD has been widely used for water purification, disinfecting in the food industry, and other industrial processes, it primarily generates ozone [45,46], as provided in SI Fig. S8, which is an undesirable byproduct for ammonia synthesis through NO_x^- chemistry. Therefore, SD is a more suitable plasma scheme for this application. In the DBD, where the gas temperature is relatively low, ozone is rapidly produced by the reaction between O atoms from electron-impact dissociation of O_2 and O_2 molecules. The energy threshold for N_2 dissociation is higher than that for O_2 [47,48], resulting in more O and less N production, and the total NO_x^- yield is insufficient.

In this instance, only some undissolved N_2O was detected.

On the other hand, the main gaseous reactive species of SD are N_2O, NO and NO_2 because the SD dissociates O_2 and N_2 molecules and produces NO_x^-, while the relatively high temperature completely inhibits the production of O_3. Our reactor design facilitates more selective production of nitrogen oxides in the SD mode. It offers the additional advantage of directly reacting the resulting intermediates with water by directly bubbling them into the water. In this case, the generated NO/NO_2 is predominantly absorbed in the liquid phase to interact with water to form acidic chemicals such as HNO_3 and HNO_2 (NO_3^- and NO_2^-, R9 to R11).

$$NO(aq) + NO_2(aq) + H_2O \leftrightarrow 2NO_2^- + 2H^+ \quad \text{(R9)}$$

$$2NO_2(aq) + H_2O \leftrightarrow NO_2^- + \quad NO_3^- + 2H^+ \quad \text{(R10)}$$

$$3NO_2^- + 3H^+ \leftrightarrow NO_3^- + 2NO(aq) + 2H_3O^+ \quad \text{(R11)}$$

$$e^- + H_2O \quad \leftrightarrow \bullet OH + H^+ \quad \text{(R12)}$$

$$\bullet OH + \bullet OH \leftrightarrow H_2O_2 \quad \text{(R13)}$$

$$NO_2(aq) + \bullet OH(aq) \leftrightarrow \quad NO_3^- + H^+ \quad \text{(R14)}$$

In our reactor design, the spark generated in the plasma bubbles enables direct interaction between the SD and water, resulting in a plasma/liquid interfacial reaction (P/L reaction). This reaction produces hydrogen ions, OH radicals, and H_2O_2, among other species, which can react with dissolved NO_2 to form NO_3^- (R12 to R14). The accumulation of ions, such as NO_3^- and NO_2^-, in plasma-activated water (PAW) can alter its physicochemical properties. The intermediates formed during the P/L reaction in the plasma bubble system play a crucial role in subsequent electrochemical conversion into ammonia. Electrochemical conditions, such as pH, nitrate/nitrite concentration, and applied potential, significantly impact the selective reduction of nitrate to ammonia [12]. Certain concentrations of protons and nitrate/nitrite ions are required to achieve high selectivity, high Faradaic efficiency, and a low overpotential for ammonia production [49]. Therefore, electrolyte engineering of PAW solutions is essential for increased productivity and selectivity in the electrocatalytic reduction of NO_x^- to ammonia.

We measured three fundamental physicochemical properties, pH, electrical conductivity, and oxidation-reduction potential (ORP), as a function of time. Fig. 4a demonstrates that after 10 min, the pH of the PAW decreased significantly from 6.92 ± 0.04–3.84 ± 0.03 and 2.75 ± 0.02 for DBD and SD, respectively. After 10-minute plasma activation, the pH reached a previously found suitable value for ammonia synthesis [12], eliminating the need for acid to adjust the pH, commonly used to increase the rate and selectivity of ammonia production [50]. Notably, the pH of the PAW treated with SD decreases significantly faster than that of DBD. This is attributed to the higher production of hydrogen ions (H^+) in the SD due to direct interaction with water. Moreover, the direct reaction of produced intermediates with water, by bubbling directly into the water, further enhances the selectivity of nitrogen oxides in the SD mode. The ability to precisely control the plasma parameters and adjust the operating conditions of the electrochemical system based on the plasma-generated species is a crucial benefit of our reactor design.

Fig. 4b shows an increasing trend of electrical conductivity of PAW over time, indicating the generation of more reactive oxygen and nitrogen species (RONS). The PAW treated with the SD mode exhibited conductivity levels ten times higher than that of DBD, consistent with the observed RONS concentrations in the PAW. The ORP values of the PAW in both discharge modes are shown in Fig. 4c. ORP measures the collective presence of oxidizing species in the PAW, including dissolved O_3, H_2O_2, H^+, NO_2^- and NO_3^-. Despite using the same pulse setup and plasma treatment duration, the ORP value was higher in the SD mode than in the DBD mode. Ultimately, the ORP values for DBD and SD were 162 mV and 193 mV, respectively. These observations suggest that the SD mode generates a higher concentration of RONS, resulting in higher

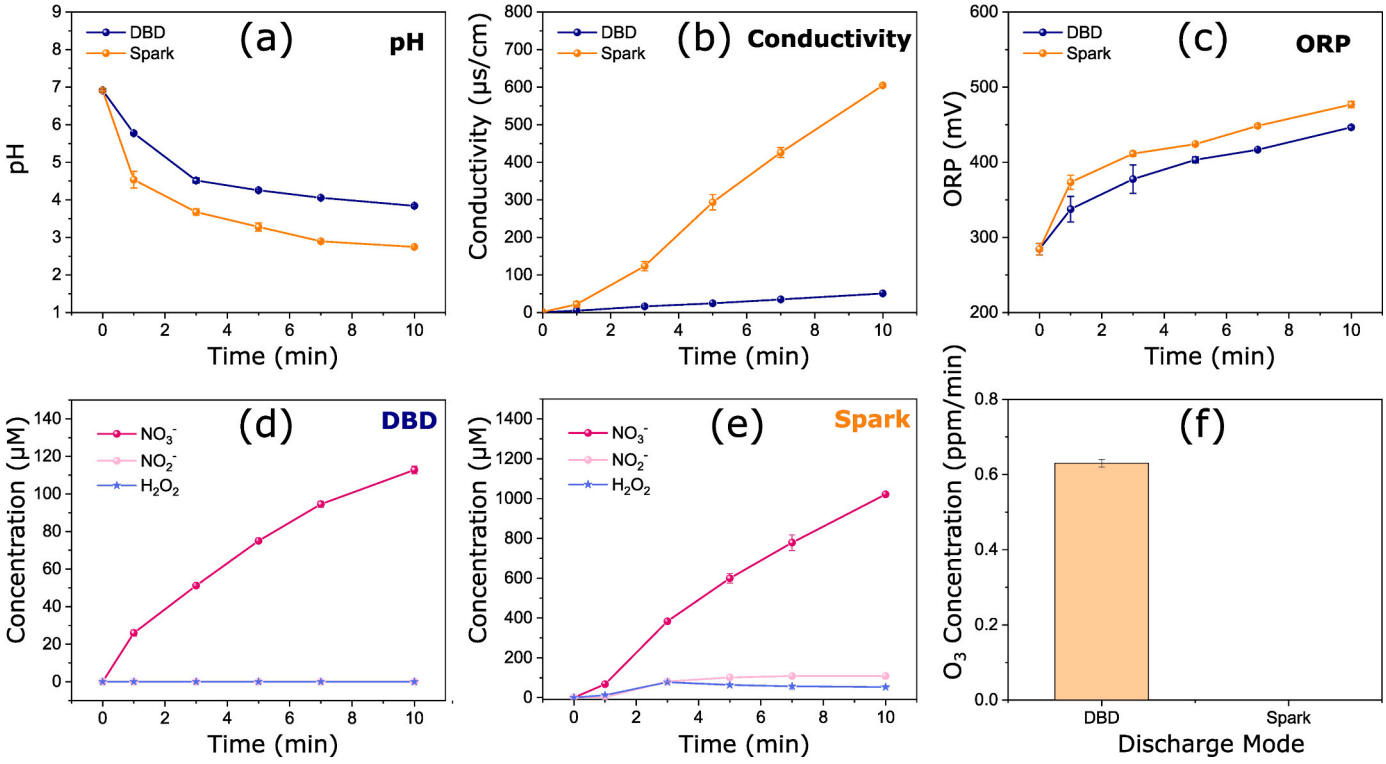

Fig. 4. Comparison of physicochemical properties between DBD and spark discharge modes as a function of plasma treatment time: (a) pH value; (b) conductivity; (c) ORP. The concentration of long-lived RONS (NO_3^-, NO_2^-, H_2O_2) as a function of plasma treatment time for (d) DBD discharge mode and (e) spark discharge mode. (f) Production rate of O_3 in the liquid phase for both DBD and spark discharge modes.

conductivity and ORP values. These findings indicate that the plasma-generated species significantly impact the physicochemical properties of PAW, which can be precisely controlled and optimized to enhance ammonia production efficiency in the subsequent electrochemical reduction process.

According to various environmental studies, plasmas in contact with liquids have been recognized as rich sources of reactive species like H_2O_2 that have extensive applications in water purification and remediation [51]. However, synthesizing ammonia via a hybrid plasma-electrocatalysis system requires a more complex approach involving gas phase chemistry, multiphase species transport, mass and heat transfer, interfacial reactions, and liquid phase chemistry. After plasma activation of air, the subsequent electrocatalytic process relies heavily on the generation of long-lived species.

To determine the concentrations of long-lived reactive oxygen and nitrogen species (RONS; NO_2^-, NO_3^-, H_2O_2) in PAW, their variation over time was measured and presented in Fig. 4(d-e). It was found that during the DBD mode, NO_2^- and H_2O_2 were not detected at any sampling point, whereas the concentration of NO_3^- increased linearly with plasma treatment time. In contrast, the SD mode generated all the tested long-lived RONS except O_3 at much higher levels (~10 times more). The concentrations of long-lived RONS (NO_2^-, NO_3^-, H_2O_2) in PAW were quantified, and their variation over time is illustrated in Fig. 4(d-e). NO_2^- and H_2O_2 were not detected at any sampling point during the DBD mode, whereas the concentration of NO_3^- increased linearly with plasma treatment time. In contrast, the SD mode generated all long-lived RONS

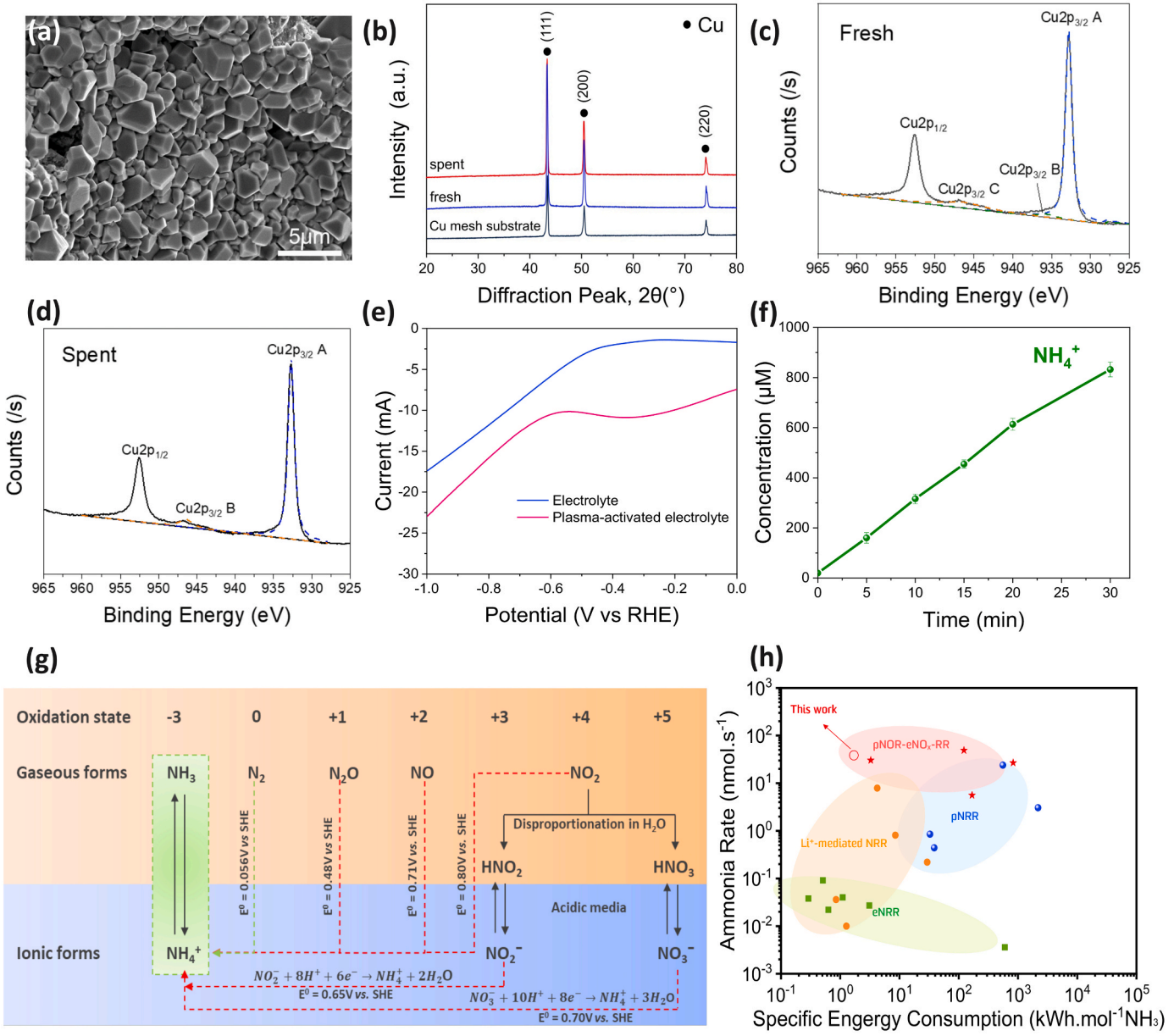

Fig. 5. Physicochemical characterizations and eNO_3RR activity of electrodes prepared – copper catalysts electrodeposited on a copper mesh for ammonia synthesis (a) Scanning electron microscopy (SEM) image. (b) XRD patterns. (c, d) high-resolution Cu 2p XPS spectra of the fresh and spent catalyst, respectively. (e) Linear sweep voltammetry (scan rate of 5 mV s^{-1}) comparing the current densities of plasma-activated electrolyte and non-plasma-activated electrolyte without stirring. (f) Ammonia production as a function of time using plasma-activated electrolyte at − 0.5 V vs. RHE. (g) Pathways towards NH_3/NH_4^+ via the electrochemical reduction of N_2, gaseous NO_x and ionic NO_x compounds with standard redox potentials (vs. standard hydrogen electrode). (h) Comparison of the energy consumption and NH_3 yield rates of this study with previously reported works covering various pathways of electrochemical nitrogen reduction (eNRR), electrochemical nitrogen oxide reduction (eNOR)-eNOx−RR, Li^+-mediated NRR, and photoelectrochemical nitrogen oxide reduction (pNOR)-eNOx−RR. Additional data can be found in Table S3.

(NO_2^-, NO_3^-, H_2O_2) at much more significant values (~ ten times more). In the SD mode, the concentration of NO_3^- increased linearly with time, while NO_2^- and H_2O_2 concentrations plateaued after 5 min. Only the DBD mode appears to have produced O_3 gas at a rate of 0.63 ± 0.01 ppm/min in the liquid phase Fig. 4(f). In the case of SD, a significant amount of H_2O_2 was made instead when plasma interfaced with water.

Addressing byproducts during nitrate production requires an understanding of the interplay between distinct discharge modes and the byproducts they produce. The DBD mode produces a substantial quantity of O_3, surpassing even the production of NO_x, which may reduce the process's effectiveness. In contrast, spark discharge produces H_2O_2, which, when balanced with acid formation, can increase NO_x solubility and, thus process efficiency. In the SD mode, the concentration of NO_3^- increased continuously over time, while NO_2^- and H_2O_2 concentrations reached a plateau after 5 mins. This indicates a balance between NO_2^- and H_2O_2 production and consumption in the production of NO_3^-.

To produce ammonia from PAW, an integrated electrochemical experiment with copper nanoparticles as the electrocatalyst was conducted. Certain metals (e.g., Cu, Ag, Pt) have a D-orbital level close to the lowest unoccupied molecular π * orbital (LUMO π *) of NO_3^-, facilitating electron transfer on these metals [52]. In the eNO_3RR process, H_2O molecules and NO_3^- ions interact with protons and are adsorbed on the electrode surface. When electric current passes through the electrode, H_2O receives the electrons and gets converted into stable adsorbed hydrogen (H_{ads}). The H_{ads} then reduces the adsorbed NO_3^- to NO_2^-, considered the rate-limiting step of eNO_3RR [53]. Subsequently, the nitrite is further reduced by H_{ads}, leading to ammonia (NH_3) formation. Among those metals, Cu stands out due to its rapid nitrate-to-nitrite conversion [54,55] and superior electrocatalytic reduction kinetics in eNO_3RR [56]. Additionally, Cu provides higher current densities and yields in highly acidic conditions [57]. Given its affordability, low hydrogen generation, and excellent conductivity, copper-based catalysts perform well in eNO_3RR [52,58–60].

Cu nanoparticles were electrodeposited on Cu mesh as the support material for this reaction. The SEM image of the Cu catalyst presented in Fig. 5a shows the existence of uniformly dispersed microcubes on the copper mesh. The crystal structure composition of the copper mesh, as synthesized electrocatalysts and spent electrocatalysts, was then determined through XRD measurements. Fig. 5b shows the normalized XRD patterns of the electrodes, revealing that each sample exhibits the XRD pattern of copper via Cu {111}, Cu {200} and Cu {220} facets. As the electrocatalyst has been electrodeposited on the top surface, we have performed an XPS analysis to gain a deeper understanding of the chemical properties of the active catalytic surface. Fig. 5c-d represents the high-resolution Cu_{2p} XPS spectra of copper catalysts before and after electrochemical ammonia synthesis. High-intensity peaks at binding energies of approximately 933 eV ($Cu^0_{2p3/2}$ or $Cu^+_{2p3/2}$) and 952.5 eV ($Cu^0_{2p1/2}$ or $Cu^+_{2p1/2}$) are observed for both samples and the copper mesh in the high-resolution spectra (Fig. S6). A weak satellite at 945 eV indicates the presence of Cu(I) oxide on the surface of the electrocatalysts. These results demonstrate the presence of metallic Cu^0 and Cu^+ in the copper nanoparticles, which persisted after the ammonia synthesis. The Cu/Cu_2O interface facilitates nitrate reduction to ammonia by promoting electron transfer at the interface, supporting the formation of the *NOH reaction intermediate. Simultaneously, it suppresses the hydrogen evolution reaction due to the higher activation energy for hydrogen production on the surface oxide than Cu metal.

The polarization curves in Fig. 5b show how the current density changes when NO_x^- is added to the electrochemical cell. The increase in current observed at approximately − 0.6 V in the absence of NO_x^- is attributed to the initiation of the hydron evolution reaction (HER). Nevertheless, the electrocatalytic NO_x^- reduction allowed for a significantly higher current density (*j*), reaching 22.5 mA cm^{-2} at 1 V vs. RHE (compared to 17.5 mA cm^{-2} for the non-plasma activated electrolyte). The electrochemical conversion of NO_x^- to ammonia involves three distinct possibilities. Both NO_2^- and NO_3^- can be directly converted to ammonia by exchanging 6 and 8 electrons, respectively, at overpotentials lower than the hydrogen generation threshold (see R 15–18). However, a pathway goes through a NO_2^- intermediary pathway to produce ammonia, also seen as a broad redox peak that appeared at around − 0.2 V to − 0.4 V vs. RHE. In our tests, five-minute sampling revealed that 85% was the FE of direct ammonia synthesis and 12% was the FE of NO_3^- to NO_2^- to ammonia. Ultimately, the combination of these pathways resulted in a monotonic increase in the concentration of NH_4^+ at a production rate of approximately 30 nmol s^{-1}, indicating the continuous conversion of NO_x^- to ammonium ions in the electrolyte (Fig. 5c). This is also supported by the ^{15}N labelling shown in Fig. S5.

$$NO_3^- + 10H^+ + 8e^- \rightarrow NH_4^+ + 3H_20,\ E^0 = 0.93V\ vs.\ RHE \quad (R15)$$

$$NO_3^- + 2H^+ + 2e^- \rightarrow NO_2^- + H_2O,\ E^0 = 1.02V\ vs.\ RHE \quad (R16)$$

$$NO_2^- + 8H^+ + 6e^- \rightarrow NH_4^+ + 2H_2O,\ E^0 = 0.86V\ vs.\ RHE \quad (R17)$$

$$2H^+ + 2e^- \rightarrow H_2,\ E^0 = 0V\ vs.\ RHE \quad (R18)$$

The electrochemical reduction of NO_3^- (NO_3RR) is a widely researched method for producing valuable chemicals, including ammonia (via 8 electrons, as depicted in Fig. 5d) [61,62]. When using the electrochemical NO_3RR reduction process, the source of NO_3^- is a critical factor for achieving productivity and appropriate techno-economics [63]. While non-plasma generated NO_3^-, such as industrial waste nitrate, has been proposed as a potential source for electrochemical ammonia production [64], the low nitrate concentrations in most nitrate sources, such as textile and power plant industrial wastewater (<10 mM) and polluted groundwater (<2 mM), pose a challenge [65]. Moreover, most highly performing electrocatalysts require highly concentrated NO_3^- electrolytes (100–1000 mM) and may not perform well in the presence of contaminants and metal impurities [50]. While recent research has shown the potential of electrocatalysis for low concentrations of nitrate to ammonia, additional and expensive costs associated with separating and concentrating nitrate solutions can add to the overall cost [66]. In contrast, plasma-generated NO_3^-, produced via pulsed NTP, allows for precise control over the concentration and other physicochemical properties by adjusting plasma parameters and duration for high-rate electroreduction and directly matching the plasma outlet to the electrolyzer.

3.2. Energy efficiency

Energy efficiency is crucial for sustainable ammonia production, as it can significantly reduce costs and enable adoption in new applications [67]. For example, sustainable ammonia has immense potential as an optimal hydrogen carrier for fuel cells, a promising decarbonizing fuel for combustion applications, and a green fertilizer source [68], but only if it can be produced with high energy efficiency. By improving the energy efficiency of the ammonia production process, the environmental impact of these industries can be significantly reduced while also ensuring a reliable and cost-effective supply for low-carbon-emitting applications. The current study has a critical advantage over other nitrogen reductions (direct and intermediary) in achieving the highest energy efficiency while maintaining a significant rate of production (as shown in Fig. 5e).

In order to gain a deeper understanding of the plasma characteristics and energy efficiency of DBD and SD discharges, we analyzed each discharge independently under identical conditions and with the same discharge power. The voltage was increased until a stable discharge was achieved, and recorded the voltage and current waveforms to observe any differences in electrical characteristics. Time-resolved waveforms of the applied voltage and discharge current were used to adjust the average discharge power. Understanding the mechanism behind plasma discharge formation is necessary to analyze both discharge modes'

energy efficiency. Our experiments demonstrated that the minimum power required to sustain both types of plasma was obtained at a frequency of 6.0 kHz, with a pulse interval of 167 ms, as illustrated in Fig. S1. These discharge parameters gave DBD a power of 1.3 watts and a $V_{p\text{-}p}$ of 12.5 ± 0.1 kV. In the case of SD, the power was 4 W, and the $V_{p\text{-}p}$ was 7.3 ± 0.1 kV.

The energy efficiency of the plasma gas activation process has been significantly impacted by the collision of electrons with heavy atoms [42]. When electrons transfer their kinetic energy to heavy atoms instead of ionizing the reactive gases, the heavy atoms absorb the energy and undergo Joule heating. This decreases the overall energy efficiency of the NO_x^- production process, as reported in the literature [42]. However, nanosecond repetitive pulsed plasma technology used in this study has shown promising results in mitigating this issue by generating high-energy bursts of electrons that enabled us to have precise control over plasma energy and pulse properties. This approach has been previously utilized in synthesizing nanomaterials, such as carbon nanotubes, where control over the synthesis process is crucial [69]. The plasma generation process can be optimized using pulses by generating plasma in short, high-energy bursts sufficient to ionize the air (O and N). After the ionization process, the ionized molecules can undergo a rest period during which they can react without plasma. This strategy increases energy efficiency and enhances the effectiveness of plasma activation. In the following section, we will evaluate the energy efficiency of NO_x^- production, the primary energy usage in the hybrid system, using this strategy for both DBD and SD discharges.

Fig. 6(a-b) shows the results of our examination, including the I-V curves used for energy consumption calculation in a typical cycle. Interestingly, each discharge mode exhibited significantly distinct waveforms. In the DBD discharge mode, the current quickly peaked during the pulse rise region and fell to zero within 500 ns. During the pulse fall time, the current reaches a negative maximum and oscillates to zero. On the other hand, the current in the spark discharge mode followed the same pattern as the DBD discharge mode for the first 200 ns before increasing and remaining constant until the pulse ended. Unexpectedly, we also observed that DBD discharge required a much higher

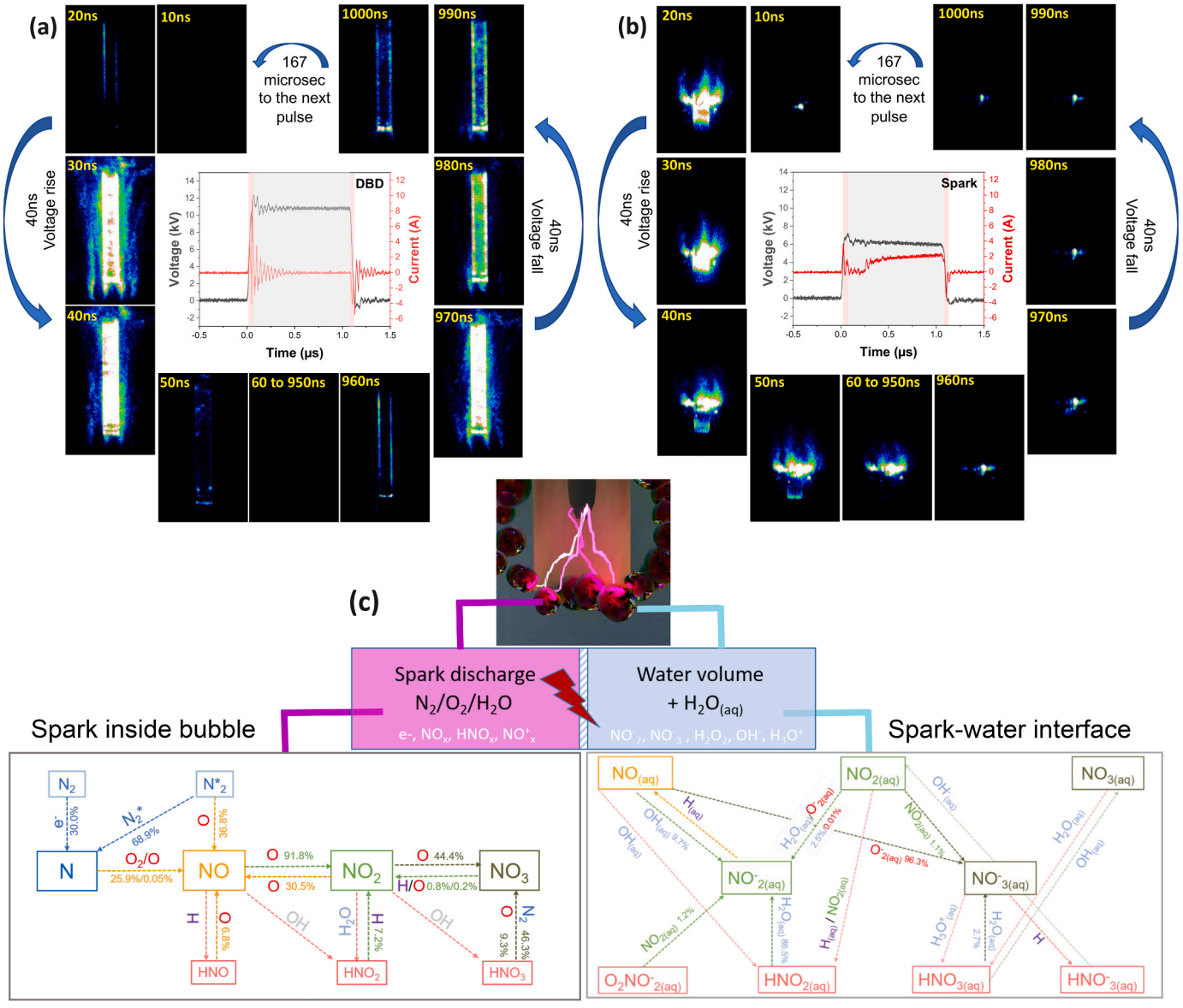

Fig. 6. Current-voltage characteristics of a single pulse with a one μs duration time and a frequency of 6.0 kHz, along with front-view ICCD images of the spatial-temporal resolved evolution process for (a) DBD discharge and (b) spark discharge. (c) Illustration of the key chemical pathways for NOx production, including sparks occurring in the gas phase within bubbles and sparks at the interfaces between bubbles and water. Note: The percentage indicates the contribution level of different reactions to produce NO_x and $NO_{x(aq)}^-$ in the gas and aqueous phase, respectively.

voltage (V_{p-p} = 12.5 ± 0.1 kV) to be initiated than the spark discharge (V_{p-p} = 7.3 ± 0.1 kV). In addition, the peak current produced by DBD discharge was 9.6 ± 0.6 A, significantly higher than the peak current produced by spark discharge, which was 3.6 ± 0.1 A. The literature has previously demonstrated that discharge at the gas-liquid interface can reduce breakdown voltage [70], supporting our observation of lower breakdown voltage in the SD mode. Furthermore, in DBD mode, the discharge power remained stable and consistent with the initial value. However, in the SD mode, the discharge power increased due to changes in conductivity in the liquid phase. The average power for the SD mode was approximately 4 ± 0.1 W, which was used for energy consumption calculations in this study.

When energy barriers are considered, the capability to calculate the energy necessary for plasma generation and, subsequently, molecular excitation in each plasma regime facilitates process optimization. The specific energy consumption for DBD and SD were determined to be 5.9 ± 0.1 kWh mol^{-1} NO_3^- and 2.7 ± 0.1 kWh mol^{-1} NO_3^-, respectively. It is worth noting that the energy consumption for DBD and spark discharges were 2.8 and 4.5 times lower, respectively, than our previous report on nitrogen fixation, where an AC power supply-NTP was used to generate NO_x^- [12]. Moreover, the spark discharge showed remarkably higher energy efficiency than the DBD discharge and, to our knowledge, the highest energy efficiency reported for any ambient nitrogen fixation via NTP (Table S2). As an illustration, the energy consumption was 2.2 times less than a multi-spark discharge system reported for ambient air activation [71], 400 times better than a plasma jet [72], and 12 times better than wire-in-nozzle spark discharge [73]. 2.1 times less than the highest reported published work, which uses DBD and water surface as the ground electrode (5.75 kWh/mol) [74].

The significant improvement in energy efficiency observed in this report was due to generating plasma in the bubbler reactor with nanosecond pulses. As the production of nitrogen oxides (NO_3^-) accounted for up to 90% of the total energy consumption in our hybrid ammonia synthesis system, this was the reason behind the highest energy efficiency reported here compared to the literature for both NO_3^- and ammonia synthesis. To better illustrate the role of short pulses in achieving such high energy efficiency, we captured front-view images of the spatial-temporal evolution of plasma discharge during each pulse and compared plasma ignition in DBD and SD discharges operating under identical conditions. The DBD ignites along the quartz tube after approximately 20 ns, and the positive rising edge discharge process lasts for around 40 ns before the plasma disappears for the following 920 ns. However, during the negative rising edge, the corresponding ICCD images showed the appearance of a second DBD ignition at a delay of 960 ns that lasted for 40 ns. This plasma on-and-off cycle during the one-microsecond pulse duration resulted from the DBD's characteristic where plasma occurs during the electric field-changing period, which was 40 ns rise and 40 ns fall in this case.

The spark discharge, in contrast, persisted continuously from 10 to 1000 ns, representing a plasma mode with high electron energy that lasts nearly the entire pulse duration. This endurance was due to the spark discharge, which remains active as long as the conduction current exists. In a fast-rising pulse, once the voltage between the electrodes surpasses a threshold (~6 kV), the spark discharge generates a conducting channel within the bubble and activates the spark-gap switch. Then, the conducting channel is quenched (pulse off), and the spark gap switch is turned off when the voltage across the electrodes and the current through the channel falls to zero. This switch can rapidly and reliably switch high voltages and currents, with nanosecond rise times (40 ns here), allowing for nitrogen ionization throughout the pulse duration (1 μs here) while minimizing collision events. In the absence of plasma (no energy input to the system), ionized nitrogen and oxygen have enough time to react as they diffuse into the water at the spark discharge and bubble interface. This process continues until the next pulse initiates a new cycle by igniting the spark.

To compare and evaluate the characteristics of DBD and spark discharges, the characteristic E/N value had to be estimated. E/N is a crucial parameter in plasma physics representing the electric field strength (E) to the number density of gas molecules (N) ratio. This parameter is essential for understanding plasma chemistry and determining the effectiveness of various plasma sources in initiating a chemical reaction [75]. Due to the difficulties of extracting representative reduced electric field E/N and the electron density (n_e) in the plasma sources with unipolar square pulse input, trial input parameters were chosen based on estimated peak current and power density to match the measurement best as shown in Table S1. For DBD, the estimated E/N and electron density were determined to be E/N 206 Td, $n_e = 2.7 \times 10^{11}$ cm^{-3}, while for SD, the electron density ranged at significantly higher values of 4.5×10^{13} cm^{-3} with significantly lower E/N as 65 Td (see Table S1 for more information). This finding further explains why SD exhibited higher productivity than DBD, primarily due to attaining high molecular energy within a very short pulse. Additionally, the plasma bubble reduced the breaking potential and resulted in much lower energy consumption than DBD.

SD offers better productivity and energy efficiency, as evidenced by a zero-D plasma kinetic model developed to gain further insight (See supporting information for detailed modelling information). High-density electrons and short residence time in spark discharge enable NO to be predominant among possible N_xO_y species (Fig. S6). Also, the model shows that the significantly lower reduced electric field in the spark discharge generates the most reactive gas species at a much higher production rate, except O_3, when compared to DBD discharge (Fig. S7).

Fig. 6c demonstrates how the spark discharge occurring within the bubble can facilitate direct interaction between the discharge and the water at the interface of the bubble. This interaction enables the effective transport of electrons and ionic species into the water. During the on time of the electron pulse, the number density of atomic N species is calculated to be significantly higher with spark discharge. Therefore, the SD initiates the interaction between atomic N and O_2, which is then enhanced by the interaction of electronically excited N_2 and atomic oxygen. The electronically excited species, in particular, N_2(A3), is shown to be important in this plasma condition with a significantly higher reaction coefficient. Additionally, SD is more efficient in maintaining a high number density of ionic species in water, such as O_2^-, OH^- or H_3O^+, due to the direct transport of electrons and ionic species through the bubble interface. Regarding nitrate and nitrite formation in water, the interaction between high-density $NO_{(aq)}$ and $O_{2(aq)}^-$ is shown to be an essential reaction in the SD facilitated by the direct interaction at the plasma-bubble interface. The significantly different water solubility of HNO_x and NO_x should be considered, particularly the effectiveness of HNO_x as a storage of synthesized NO_x from the gas discharge when it is to be transferred to the water. The solubility of HNO, HNO_2 and HNO_3 is much higher than that of NO_x species. As a result, $HNO_{2(aq)}$ contributes the most to the production of nitrite in water under spark discharge conditions. In contrast, In DBD conditions, most reactive radicals and ionic species tend to recombine into stable molecules while being transported through the remote plasma area between the active DBD discharge volume and water.

4. Conclusions

In conclusion, the benefits of combining plasma, liquids and electrocatalysis are becoming more and more evident. Developing a nanosecond pulse-driven plasma bubble reactor with multiple discharge configurations is an innovative method for facilitating the electrochemical production of ammonia in a sustainable manner. The unique advantage of the plasma bubble approach developed here is that it enables a large volume of plasma in water/liquids with decreased breakdown voltage and energy consumption. In addition to maintaining performance and energy efficiency at scale, the process is scalable in three dimensions. In plasma engineering, scalability is the ability to achieve larger or smaller scale production by adjusting individual

productivity or unit numbers, and does not follow a linear scaling relationship between the production rate and voltage/current. Maintaining a small- to medium-scale optimized plasma reactor and constructing an array of units is the most straightforward method. Therefore, multiple reactors can be utilized in parallel. Considering the potential for effective scaling in three dimensions and the performance of plasma bubbles (in terms of production rates and energy efficiency), this is a very efficient approach, especially in plasma-assisted electrochemical conversion. Consequently, plasma-bubble reactors can be integrated into a flow system, allowing for continuous ammonia production when appropriate electrocatalysts, such as the copper nanoparticles developed in this study, are used. Therefore, this strategy breaks down the nitrogen conversion process into NO_3^- formation and NO_3^- reduction. This separation permits us to independently investigate, refine, and scale up each stage. Notably, neither of these stages is the rate-determining step, as our plasma reactor is scalable to match the size and output capabilities of the electrolyzer and vice versa. This unique adaptability guarantees that neither stage hinders the overall process rate.

To this end, the research presented in this study has demonstrated a deep investigation of two plasma-bubble discharge modes, DBD and SD, and the management of energy mapping for both modes. However, attaining sufficient molecular energy in each short pulse was essential to allow nitrogen oxidation to achieve high productivity. The investigation has revealed that SD is the preferred mode for NO_3^- production in the liquid phase due to its higher energy density, achieving the energy efficiency of 2.7 ± 0.1 kWh mol^{-1} NO_3^-. The ability of the on-and-off plasma ignition cycle to regulate energy input for ionization and production of nitrogen oxides was the key to the high energy efficiency observed here. Even with a very short pulse on time of 1 ms out of an entire period of 167 ms, still a high production of NO of approximately 1.9 ms mol s^{-1} of NO_x in gas volume was observed. The zero-dimensional plasma chemistry model indicates that high-density $NO_{x\,(aq)}$ production in water is significantly more efficient with spark discharge than with DBD. This is primarily due to the increased NO_x synthesis within the gas discharge volume, facilitated by high-density electrons that persist for extended periods. Additionally, transporting electrons, ions, and reactive chemical species from the discharge volume to the liquid water domain is more efficient in a spark discharge. Furthermore, the nitrate and nitrite formation mechanisms are significantly different between spark discharge and DBD conditions. The former is more effective due to direct interaction at the plasma-bubble interface. While nanosecond pulsed plasma has been widely used in DBD mode for ozone production, the current research indicates that high productivity and energy efficiency in nitrate synthesis can only be achieved through the spark in a bubble, which interfaces directly with water. These findings represent significant progress towards advancing plasma-driven electrochemical synthesis for sustainable ammonia production, with potential applications as a hydrogen carrier for the emerging global hydrogen economy.

Author contributions

The study was conceptualized and supervised by A. R. J. and R. Z.. R. A. contributed with student supervision and data validation. J. S. carried out the majority of the experiments, analyzed the data, and wrote the first draft. The final draft was written by A. R. J.. J. H. did the modelling and related analysis. Discussions and data analysis were assisted by Y. G., Z. Q., Z. L., D. L., T. Z., K. O., P. C. and E. L.. All authors contributed to the review and editing of the manuscript and interpretation of the results.

Declaration of Competing Interest

Authors P. Cullen, E. Lovell, K. Ostrikov, A. R. Jalili, and T. Zhang are associated with PlasmaLeap Technologies, the provider of the plasma-bubble reactors used in this study.

Data Availability

Data will be made available on request.

Acknowledgements

The Australian Research Council financially supported this work under the Discovery Early Career Research Award to A. R. Jalili. (DE180100215). This work is partly supported by the National Natural Science Foundation of China (Grant No. 52377160). K.O. thanks the Australian Research Council (ARC) and QUT Centre for Materials Science for partial support.

Supplementary data

Supplementary materials to this article can be found online.

Appendix A. Supporting information

Supplementary data associated with this article can be found in the online version at doi:10.1016/j.apcatb.2023.123426.

References

[1] J.W. Erisman, M.A. Sutton, J. Galloway, Z. Klimont, W. Winiwarter, How a century of ammonia synthesis changed the world, Nat. Geosci. 1 (2008) 636–639.
[2] R.M. Nayak-Luke, R. Bañares-Alcántara, Techno-economic viability of islanded green ammonia as a carbon-free energy vector and as a substitute for conventional production, Energy Environ. Sci. 13 (2020) 2957–2966.
[3] L.K. Boerner, Industrial ammonia production emits more CO_2 than any other chemical-making reaction. Chemists want to change that, Chem. Eng. N. 97 (2019) 1–9.
[4] D.R. MacFarlane, P.V. Cherepanov, J. Choi, B.H. Suryanto, R.Y. Hodgetts, J. M. Bakker, F.M.F. Vallana, A.N. Simonov, A roadmap to the ammonia economy, Joule 4 (2020) 1186–1205.
[5] S. Ghavam, M. Vahdati, I. Wilson, P. Styring, Sustainable ammonia production processes, Front. Energy Res. 34 (2021).
[6] D. Zhou, R. Zhou, R. Zhou, B. Liu, T. Zhang, Y. Xian, P.J. Cullen, X. Lu, K. K. Ostrikov, Sustainable ammonia production by non-thermal plasmas: status, mechanisms, and opportunities, Chem. Eng. J. 421 (2021), 129544.
[7] J. Choi, H.-L. Du, C.K. Nguyen, B.H. Suryanto, A.N. Simonov, D.R. MacFarlane, Electroreduction of nitrates, nitrites, and gaseous nitrogen oxides: a potential source of ammonia in dinitrogen reduction studies, ACS Energy Lett. 5 (2020) 2095–2097.
[8] D.R. MacFarlane, J. Choi, B.H. Suryanto, R. Jalili, M. Chatti, L.M. Azofra, A. N. Simonov, Liquefied sunshine: Transforming renewables into fertilizers and energy carriers with electromaterials, Adv. Mater. 32 (2020) 1904804.
[9] T. Zhang, R. Zhou, S. Zhang, R. Zhou, J. Ding, F. Li, J. Hong, L. Dou, T. Shao, A. B. Murphy, Sustainable ammonia synthesis from nitrogen and water by one-step plasma catalysis, Energy Environ. Mater. (2022).
[10] K.H. Rouwenhorst, Y. Engelmann, K. van't Veer, R.S. Postma, A. Bogaerts, L. Lefferts, Plasma-driven catalysis: green ammonia synthesis with intermittent electricity, Green. Chem. 22 (2020) 6258–6287.
[11] P. Peng, P. Chen, C. Schiappacasse, N. Zhou, E. Anderson, D. Chen, J. Liu, Y. Cheng, R. Hatzenbeller, M. Addy, A review on the non-thermal plasma-assisted ammonia synthesis technologies, J. Clean. Prod. 177 (2018) 597–609.
[12] J. Sun, D. Alam, R. Daiyan, H. Masood, T. Zhang, R. Zhou, P.J. Cullen, E.C. Lovell, A.R. Jalili, R. Amal, A hybrid plasma electrocatalytic process for sustainable ammonia production, Energy Environ. Sci. 14 (2021) 865–872.
[13] J. Hong, T. Zhang, R. Zhou, R. Zhou, K.K. Ostikov, A. Rezaeimotlagh, P.J. Cullen, Plasma bubbles: a route to sustainable chemistry, AAPPS Bull. 31 (2021) 1–14.
[14] J. Liang, Z. Li, L. Zhang, X. He, Y. Luo, D. Zheng, Y. Wang, T. Li, H. Yan, B. Ying, Advances in ammonia electrosynthesis from ambient nitrate/nitrite reduction, Chem (2023).
[15] A. Wu, J. Yang, B. Xu, X.-Y. Wu, Y. Wang, X. Lv, Y. Ma, A. Xu, J. Zheng, Q. Tan, Direct ammonia synthesis from the air via gliding arc plasma integrated with single atom electrocatalysis, Appl. Catal. B: Environ. 299 (2021), 120667.
[16] Y. Cui, H. Yang, C. Dai, P. Ren, C. Song, X. Ma, Coupling of $LaFeO_3$–plasma catalysis and $Cu+/Cu^0$ electrocatalysis for direct ammonia synthesis from air, Ind. Eng. Chem. Res. 61 (2022) 4816–4823.
[17] L. Li, C. Tang, X. Cui, Y. Zheng, X. Wang, H. Xu, S. Zhang, T. Shao, K. Davey, S. Z. Qiao, Efficient nitrogen fixation to ammonia through integration of plasma oxidation with electrocatalytic reduction, Angew. Chem. 133 (2021) 14250–14256.
[18] S. Zhang, L. Zong, X. Zeng, R. Zhou, Y. Liu, C. Zhang, J. Pan, P.J. Cullen, K. K. Ostrikov, T. Shao, Sustainable nitrogen fixation with nanosecond pulsed spark

discharges: insights into free-radical-chain reactions, Green Chem. 24 (2022) 1534–1544.
[19] C. Man, C. Zhang, H. Fang, R. Zhou, B. Huang, Y. Xu, X. Zhang, T. Shao, Nanosecond-pulsed microbubble plasma reactor for plasma-activated water generation and bacterial inactivation, Plasma Process. Polym. (2022), e2200004.
[20] M. Qi, X. Zhang, S. Peng, R. Fan, B. Pang, R. Luo, Z. Ding, D. Xu, D. Liu, Nanosecond-pulsed plasma jet in air and air/helium mixtures: Plasma properties and anticancer effect, Phys. Plasmas 30 (2023), 033512.
[21] D.Z. Pai, D.A. Lacoste, C.O. Laux, Transitions between corona, glow, and spark regimes of nanosecond repetitively pulsed discharges in air at atmospheric pressure, J. Appl. Phys. 107 (2010), 093303.
[22] T.L. Chng, A. Brisset, P. Jeanney, S. Starikovskaia, I. Adamovich, P. Tardiveau, Electric field evolution in a diffuse ionization wave nanosecond pulse discharge in atmospheric pressure air, Plasma Sources Sci. Technol. 28 (2019) 09LT02.
[23] C. Man, C. Zhang, H. Fang, R. Zhou, B. Huang, Y. Xu, X. Zhang, T. Shao, Nanosecond-pulsed microbubble plasma reactor for plasma-activated water generation and bacterial inactivation, Plasma Process. Polym. 19 (2022) 2200004.
[24] M.A. Malik, K.H. Schoenbach, T.M. Abdel-Fattah, R. Heller, C. Jiang, Low cost compact nanosecond pulsed plasma system for environmental and biomedical applications, Plasma Chem. Plasma Process. 37 (2017) 59–76.
[25] X. Cui, J. Shen, Y. Zhou, X. Zhu, R. Zhou, R. Zhou, Z. Fang, P.J. Cullen, Nanosecond pulse-driven atmospheric-pressure plasmas for polymer surface modifications: Wettability performance, insulation evaluation and mechanisms, Appl. Surf. Sci. 597 (2022), 153640.
[26] X. Qing, L. Haofan, S. Zhang, W. Ruixue, K. Fei, S. Tao, Deposition of SiCxHyOz thin film on epoxy resin by nanosecond pulsed APPJ for improving the surface insulating performance, Plasma Sci. Technol. 20 (2017), 025504.
[27] H. Cheng, J. Fan, Y. Zhang, D. Liu, K.K. Ostrikov, Nanosecond pulse plasma dry reforming of natural gas, Catal. Today 351 (2020) 103–112.
[28] X. Wang, Y. Gao, S. Zhang, H. Sun, J. Li, T. Shao, Nanosecond pulsed plasma assisted dry reforming of CH4: The effect of plasma operating parameters, Appl. Energy 243 (2019) 132–144.
[29] S. Zhang, G. Yuan, S. Hao, F. Zhe, S. Tao, Charge transfer in plasma assisted dry reforming of methane using a nanosecond pulsed packed-bed reactor discharge, Plasma Sci. Technol. 23 (2021), 064007.
[30] R.J. Wandell, H. Wang, R.K. Bulusu, R.O. Gallan, B.R. Locke, Formation of nitrogen oxides by nanosecond pulsed plasma discharges in gas–liquid reactors, Plasma Chem. Plasma Process. 39 (2019) 643–666.
[31] Z. Wang, L. Liu, D. Liu, M. Zhu, J. Chen, J. Zhang, F. Zhang, J. Jiang, L. Guo, X. Wang, Combination of NO_x mode and O_3 mode air discharges for water activation to produce a potent disinfectant, Plasma Sources Sci. Technol. 31 (2022) 05LT01.
[32] S. Pancheshnyi, B. Eismann, G. Hagelaar, L. Pitchford, Computer code zdplaskin, University of Toulouse, LAPLACE, tech. rep, CNRS-UPS-INP, Toulouse, France, 2008.
[33] J. Hong, T. Zhang, R. Zhou, L. Dou, S. Zhang, R. Zhou, B. Ashford, T. Shao, A.B. Murphy, K.K. Ostrikov, Green chemical pathway of plasma synthesis of ammonia from nitrogen and water: a comparative kinetic study with a N_2/H_2 system, (2022).
[34] W. Ning, J. Lai, J. Kruszelnicki, J.E. Foster, D. Dai, M.J. Kushner, Propagation of positive discharges in an air bubble having an embedded water droplet, Plasma Sources Sci. Technol. 30 (2021), 015005.
[35] G. Hagelaar, L.C. Pitchford, Solving the Boltzmann equation to obtain electron transport coefficients and rate coefficients for fluid models, Plasma Sources Sci. Technol. 14 (2005) 722.
[36] A.M. Lietz, M.J. Kushner, Air plasma treatment of liquid covered tissue: long timescale chemistry, J. Phys. D: Appl. Phys. 49 (2016), 425204.
[37] F. Peeters, M. Van de Sanden, The influence of partial surface discharging on the electrical characterization of DBDs, Plasma Sources Sci. Technol. 24 (2014), 015016.
[38] J. Hong, M. Aramesh, O. Shimoni, D.H. Seo, S. Yick, A. Greig, C. Charles, S. Prawer, A.B. Murphy, Plasma catalytic synthesis of ammonia using functionalized-carbon coatings in an atmospheric-pressure non-equilibrium discharge, Plasma Chem. Plasma Process. 36 (2016) 917–940.
[39] F. Iza, J.L. Walsh, M.G. Kong, From submicrosecond-to nanosecond-pulsed atmospheric-pressure plasmas, IEEE Trans. Plasma Sci. 37 (2009) 1289–1296.
[40] S. Keller, P. Rajasekaran, N. Bibinov, P. Awakowicz, Characterization of transient discharges under atmospheric-pressure conditions applying nitrogen photoemission and current measurements, J. Phys. D: Appl. Phys. 45 (2012), 125202.
[41] P. Bruggeman, N. Sadeghi, D. Schram, V. Linss, Gas temperature determination from rotational lines in non-equilibrium plasmas: a review, Plasma Sources Sci. Technol. 23 (2014), 023001.
[42] S. Zhang, W. Wang, L. Jia, Z. Liu, Y. Yang, L. Dai, Rotational, vibrational, and excitation temperatures in bipolar nanosecond-pulsed diffuse dielectric-barrier-discharge plasma at atmospheric pressure, IEEE Trans. Plasma Sci. 41 (2012) 350–354.
[43] S. Huang, T. Li, Z. Zhang, P. Ma, Rotational and vibrational temperatures in the spark plasma by various discharge energies and strategies, Appl. Energy 251 (2019), 113358.
[44] W. Wang, B. Patil, S. Heijkers, V. Hessel, A. Bogaerts, Nitrogen fixation by gliding arc plasma: better insight by chemical kinetics modelling, ChemSusChem 10 (2017) 2145–2157.
[45] N. Jiang, L. Guo, C. Qiu, Y. Zhang, K. Shang, N. Lu, J. Li, Y. Wu, Reactive species distribution characteristics and toluene destruction in the three-electrode DBD reactor energized by different pulsed modes, Chem. Eng. J. 350 (2018) 12–19.
[46] C. Aggelopoulos, S. Meropoulis, M. Hatzisymeon, Z. Lada, G. Rassias, Degradation of antibiotic enrofloxacin in water by gas-liquid nsp-DBD plasma: Parametric analysis, effect of H_2O_2 and CaO_2 additives and exploration of degradation mechanisms, Chem. Eng. J. 398 (2020), 125622.
[47] K. Liu, W. Geng, X. Zhou, Q. Duan, Z. Zheng, K. Ostrikov, Transition mechanisms between selective O_3 and NO_x generation modes in atmospheric-pressure plasmas: decoupling specific discharge energy and gas temperature effects, Plasma Sources Science and Technology, 2023.
[48] M.A. Malik, C. Jiang, R. Heller, J. Lane, D. Hughes, K.H. Schoenbach, Ozone-free nitric oxide production using an atmospheric pressure surface discharge–a way to minimize nitrogen dioxide co-production, Chem. Eng. J. 283 (2016) 631–638.
[49] J.M. McEnaney, S.J. Blair, A.C. Nielander, J.A. Schwalbe, D.M. Koshy, M. Cargnello, T.F. Jaramillo, Electrolyte engineering for efficient electrochemical nitrate reduction to ammonia on a titanium electrode, ACS Sustain. Chem. Eng. 8 (2020) 2672–2681.
[50] H. Xu, Y. Ma, J. Chen, W.-x Zhang, J. Yang, Electrocatalytic reduction of nitrate–a step towards a sustainable nitrogen cycle, Chem. Soc. Rev. (2022).
[51] P. Bruggeman, M.J. Kushner, B.R. Locke, J.G. Gardeniers, W. Graham, D.B. Graves, R. Hofman-Caris, D. Maric, J.P. Reid, E. Ceriani, Plasma–liquid interactions: a review and roadmap, Plasma Sources Sci. Technol. 25 (2016), 053002.
[52] S. Garcia-Segura, M. Lanzarini-Lopes, K. Hristovski, P. Westerhoff, Electrocatalytic reduction of nitrate: Fundamentals to full-scale water treatment applications, Appl. Catal. B: Environ. 236 (2018) 546–568.
[53] L. Mattarozzi, S. Cattarin, N. Comisso, R. Gerbasi, P. Guerriero, M. Musiani, E. Verlato, Electrodeposition of compact and porous Cu-Pd alloy layers and their application to nitrate reduction in alkali, Electrochim. Acta 230 (2017) 365–372.
[54] G. Dima, A. De Vooys, M. Koper, Electrocatalytic reduction of nitrate at low concentration on coinage and transition-metal electrodes in acid solutions, J. Electroanal. Chem. 554 (2003) 15–23.
[55] J.F. Su, I. Ruzybayev, I. Shah, C. Huang, The electrochemical reduction of nitrate over micro-architectured metal electrodes with stainless steel scaffold, Appl. Catal. B: Environ. 180 (2016) 199–209.
[56] J. Li, H. Liu, F. Du, L. Liu, Y. Gu, C. Li, C. Guo, H. Wang, Microenvironmental corrosion and hydrolysis induced two-dimensional heterojunction of copper oxide@ ferriferrous oxide for efficient electrochemical nitrate reduction to ammonia, Chem. Eng. J. 471 (2023), 144488.
[57] N. Aouina, H. Cachet, C. Debiemme-Chouvy, T.T.M. Tran, Insight into the electroreduction of nitrate ions at a copper electrode, in neutral solution, after determination of their diffusion coefficient by electrochemical impedance spectroscopy, Electrochim. Acta 55 (2010) 7341–7345.
[58] C. Roy, J. Deschamps, M. Martin, E. Bertin, D. Reyter, S. Garbarino, L. Roué, D. Guay, Identification of Cu surface active sites for a complete nitrate-to-nitrite conversion with nanostructured catalysts, Appl. Catal. B: Environ. 187 (2016) 399–407.
[59] G.-F. Chen, Y. Yuan, H. Jiang, S.-Y. Ren, L.-X. Ding, L. Ma, T. Wu, J. Lu, H. Wang, Electrochemical reduction of nitrate to ammonia via direct eight-electron transfer using a copper–molecular solid catalyst, Nat. Energy 5 (2020) 605–613.
[60] Y. Wang, W. Zhou, R. Jia, Y. Yu, B. Zhang, Unveiling the activity origin of a copper-based electrocatalyst for selective nitrate reduction to ammonia, Angew. Chem. Int. Ed. 59 (2020) 5350–5354.
[61] G. Qing, R. Ghazfar, S.T. Jackowski, F. Habibzadeh, M.M. Ashtiani, C.-P. Chen, M. R. Smith III, T.W. Hamann, Recent advances and challenges of electrocatalytic N2 reduction to ammonia, Chem. Rev. 120 (2020) 5437–5516.
[62] Y. Ren, C. Yu, L. Wang, X. Tan, Z. Wang, Q. Wei, Y. Zhang, J. Qiu, Microscopic-level insights into the mechanism of enhanced NH3 synthesis in plasma-enabled cascade N2 oxidation–electroreduction system, J. Am. Chem. Soc. 144 (2022) 10193–10200.
[63] R. Daiyan, T. Tran-Phu, P. Kumar, K. Iputera, Z. Tong, J. Leverett, M.H.A. Khan, A. A. Esmailpour, A. Jalili, M. Lim, Nitrate reduction to ammonium: from CuO defect engineering to waste NO_x-to-NH_3 economic feasibility, Energy Environ. Sci. 14 (2021) 3588–3598.
[64] J. Theerthagiri, J. Park, H.T. Das, N. Rahamathulla, E.S. Cardoso, A.P. Murthy, G. Maia, D.V.N. Vo, M.Y. Choi, Electrocatalytic conversion of nitrate waste into ammonia: a review, Environ. Chem. Lett. 20 (2022) 2929–2949.
[65] P.H. van Langevelde, I. Katsounaros, M.T. Koper, Electrocatalytic nitrate reduction for sustainable ammonia production, Joule 5 (2021) 290–294.
[66] K.-H. Kim, H. Lee, X. Huang, J.H. Choi, C. Chen, J.K. Kang, D. O'Hare, Energy-efficient electrochemical ammonia production from dilute nitrate solution, Energy Environ. Sci. 16 (2023) 663–672.
[67] X. Zeng, S. Zhang, Y. Liu, X. Hu, K.K. Ostrikov, T. Shao, Energy-efficient pathways for pulsed-plasma-activated sustainable ammonia synthesis, ACS Sustain. Chem. Eng. (2023).
[68] P. Wolfram, P. Kyle, X. Zhang, S. Gkantonas, S. Smith, Using ammonia as a shipping fuel could disturb the nitrogen cycle, Nat. Energy 7 (2022) 1112–1114.
[69] D.Z. Pai, K. Ostrikov, S. Kumar, D.A. Lacoste, I. Levchenko, C.O. Laux, Energy efficiency in nanoscale synthesis using nanosecond plasmas, Sci. Rep. 3 (2013) 1221.
[70] X. Lu, S. Wang, R. Zhou, Z. Fang, P. Cullen, Discharge modes and liquid interactions for plasma-bubble discharges, J. Appl. Phys. 132 (2022), 073303.
[71] T. Nakaso, T. Harigai, S.A. Kusumawan, T. Shimomura, T. Tanimoto, Y. Suda, H. Takikawa, Multi-spark discharge system for preparation of nutritious water. AIP Conference Proceedings, AIP Publishing LLC, 2018, 020016.
[72] K. Ogawa, J.-S. Oh, N. Gaur, S.-H. Hong, H. Kurita, A. Mizuno, A. Hatta, R.D. Short, M. Ito, E.J. Szili, Modulating the concentrations of reactive oxygen and nitrogen species and oxygen in water with helium and argon gas and plasma jets, Jpn. J. Appl. Phys. 58 (2018) SAAB01.

[73] K. Tachibana, T. Nakamura, Comparative study of discharge schemes for production rates and ratios of reactive oxygen and nitrogen species in plasma activated water, J. Phys. D: Appl. Phys. 52 (2019), 385202.

[74] N.C. Roy, N. Maira, C. Pattyn, A. Remy, M.-P. Delplancke, F. Reniers, Mechanisms of reducing energy costs for nitrogen fixation using air-based atmospheric DBD plasmas over water in contact with the electrode, Chem. Eng. J. (2023), 141844.

[75] D.A. Gurnett, A. Bhattacharjee, Introduction to plasma physics: with space and laboratory applications, Cambridge University Press, 2005.